



http://pubs.acs.org/journal/acsodf Article

# Experimental and Simulation Studies on Nonwoven Polypropylene— Nitrile Rubber Blend: Recycling of Medical Face Masks to an Engineering Product

George Varghese P. J, Deepthi Anna David, Anas Karuth, Jabeen Fatima Manamkeri Jafferali, Sabura Begum P. M, Jinu Jacob George, Bakhtiyor Rasulev,\* and Prasanth Raghavan\*



Cite This: ACS Omega 2022, 7, 4791-4803



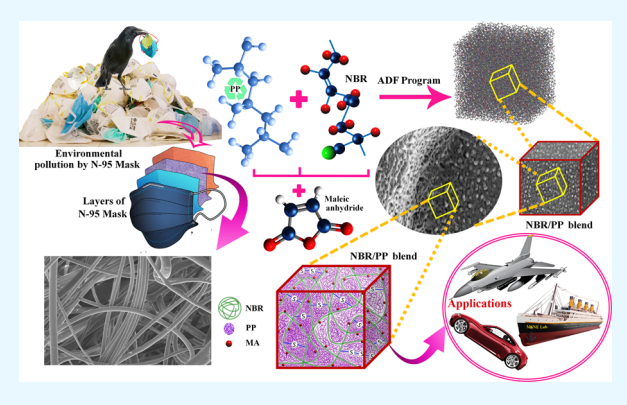
**ACCESS** I

III Metrics & More

Article Recommendations

Supporting Information

ABSTRACT: The battle against the COVID-19 pandemic counters the waste management system, as billions of single-use face masks are used per day all over the world. Proper disposal of used face masks without jeopardizing the health and the environment is a challenge. Herein, a novel method for recycling of medical face masks has been studied. This method incorporates the nonwoven polypropylene (PP) fiber, which is taken off from the mask after disinfecting it, with acrylonitrile butadiene rubber (NBR) using maleic anhydride as the compatibilizer, which results in a PP–NBR blend with a high percentage economy. The PP–NBR blends show enhanced thermomechanical properties among which, 70 wt % PP content shows superior properties compared to other composites with 40, 50, and 60 wt % of PP. The fully Atomistic simulation of PP-NBR blend with compatibilizer shows an improved tensile and barrier properties, which



is in good agreement with the experimental studies. The molecular dynamics simulation confirms that the compatibility between non-polar PP and polar NBR phases are vitally important for increasing the interfacial adhesion and impeding the phase separation.

## 1. INTRODUCTION

The 21st century emerged like a roller-coaster for humankind. One of the most unexpected jeopardies aroused as the COVID-19 pandemic, caused by the novel coronavirus, which spreads from an infected person to the others causingin severe acute respiratory syndrome, from which a myriad of people are suffering. The voyage of COVID-19 pandemic has created a jolt, and the manifestation of the cure is on its way. Simultaneously, this has escalated the use of surgical face masks in the medical field and even by the common people, which indicates that billions of waste is generated each day all over the world.<sup>1,2</sup> The tribulation created by the utmost surge in the production and usage of medical face masks has led the scientific world to look for an effective remedy to dispose the used face masks without directing them to the nasty plastic pollution. As a foresight, the detrimental consequences of the incautious discarding (Figure 1) of the used face masks will significantly affect the environment, especially through soil and water contamination. Moreover, the used face masks, which are heedlessly thrown away, can become the medium for the propagation of the infectious disease, which leads to uncontrollable spread of the coronavirus. Incineration of masks being the potential choice, burning of huge amount of plastic wastes will result in extreme carbon emission, causing air pollution and thereby extreme climatic change. 3-6 The crux

of the matter is the proper disposal of the face masks without having a negative impact on the environment as well as on the health of people.

The recycling of used disposable medical face masks is the only predominant strategy to completely avoid the consequences of plastic pollution. However, some sort of effort is required to adopt a potential recycling method.<sup>7–9</sup> The materials used for the production of disposable face masks can be categorized and recycled. Medical masks, especially the N95 mask, is a multi-layered mask, with a high filtration efficiency of at least 95% and permissible pressure drop. It consists of nonwoven polypropylene (PP) inner filtration layer, which is mainly prepared by the melt blowing technique that helps to filter out the smallest particles, including dust, vapors, coronavirus, and other airborne microorganisms, preventing them from getting into the next layer. The N95 mask consists of a waterproof nonwoven fabric followed by inner filtration

Received: September 6, 2021 Accepted: December 8, 2021 Published: January 18, 2022

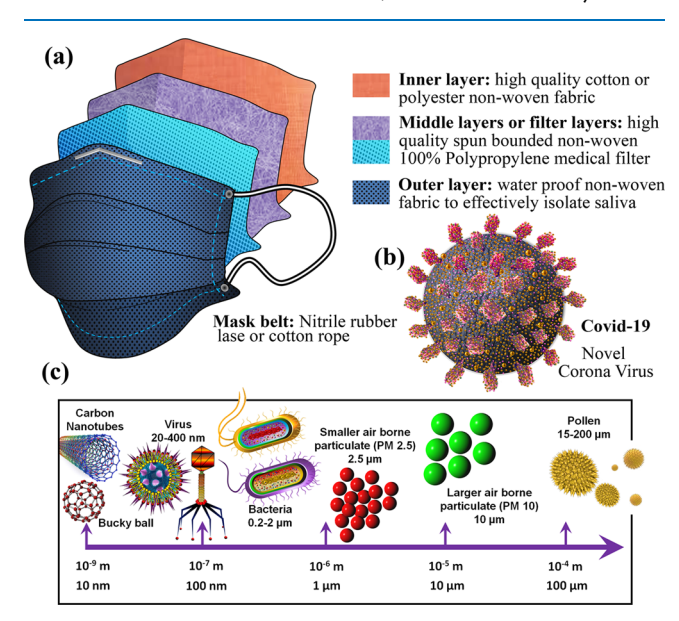






Figure 1. Improperly disposed used face masks and their collection.

layers of high-quality spun bounded nonwoven PP with a good filtration efficiency and an inner layer of cotton nonwoven fiber. The transformation of these medical wastes into a useful product demands the adoption of a potential method. The structure of the N95 face mask, the novel coronavirus, and the size range of particulates that can be filtered out by the PP inner filtration layer in the N95 face mask are shown in Figure 2. The mask can be disinfected first, and the PP filter layers can



**Figure 2.** Schematic representation of the structure of: (a) multilayered N95 face mask, (b) novel coronavirus with a spherical crownlike shape with spikes, and (c) size range of the particles that can be effectively trapped within the N95 face mask.

be separated and shredded. There are various strategies for disinfecting and reusing the medical face masks by adopting some acceptable techniques like UV illumination, air drying for over 72 h, hydrogen peroxide vaporization, and thermal and spray-on surface disinfection. <sup>10–13</sup>

Looking on the trajectories of research done on recycling of PP, a few studies have been conducted on the disposal of face masks, out of which the most common is recycling. Crespo et al. <sup>14</sup> studied the recycling of medical face masks using the melt mixing process, and the final blend can be used to make flower pots, toys, garbage bins, and so forth, in which technical specifications are not considered. Battegazzore et al. <sup>7</sup> reported the mechanical recycling of medical face masks in which different combinations of the components of the face masks

were melt mixed in an extruder at a high temperature and their properties were studied. Likewise, efforts on the recycling of PP to make decorative bricks, face shields, and so forth are also counted, which are not scientifically reported. Apart from these recycling processes, the current study focusses on a hybrid system fortified with the strength of PP along with the elasticity of a synthetic rubber that can be used for a wide range of engineering applications like car bumpers and so forth, focusing on the high impact property.

In this scenario, apart from the trajectories of research done on the recycling of used disposable medical face masks, the current study focuses on a novel method for the recycling of used medical face masks to make a value-added engineering product that can be used for a wide range of applications. A blend of PP with acrylonitrile butadiene rubber (NBR), commonly known as nitrile rubber, is prepared, in which PP is taken out only after proper disinfection of the mask. PP is a non-polar material with excellent resistance to heat, moisture, and extreme weather conditions; is mechanically strong and chemically inert; and has a high-volume resistivity, highfrequency insulating property, and high abrasion resistance. NBR is a polar synthetic rubber and a copolymer of acrylonitrile (ACN) and butadiene monomers with extraordinary oil resistance, moderate tensile strength and abrasion resistance, good heat and chemical resistance, high electrical conductivity, and low temperature flexibility. 16 An increase in the ACN content will result in a dramatic change in the properties of the NBR matrix. 17,18 Unequivocally, the properties of the PP-NBR blend would be a drastic combination of the properties of both PP and NBR, which can be used for various applications. 19-21 In parallel with experiments, computational assessment and prediction of polymeric properties have become increasingly demanding to accelerate the design and development of polymeric blends and composites. The combination of data-driven methods and molecular dynamics simulations provides valuable insights into the physical mechanisms of polymers at the molecular level.<sup>22,23</sup> The molecular dynamics simulation of polymeric blends provides a clear information about the stress-strain and transportation characteristics of the blends.<sup>24,25</sup>

The challenge would be the incompatibility of non-polar PP with polar NBR. The immiscible PP–NBR blends can be made compactible by using a compatibilizer that can act as a bridge between the PP and the NBR matrix. The compatibilizer used in the current study is maleic anhydride (MA), which is an organic compound that can act as an interfacial agent by reacting with PP using dicumyl peroxide (DCP) and further react with NBR. <sup>26–28</sup> NBR is cured by conventional sulfur

vulcanization separately with the help of activators, accelerators, and other additives. The reactive compatibilization technique results in PP–NBR blends with extraordinary properties and the creation of an engineering product from the trash for astonishing applications. Moreover, as an advantage, the process used in this study is energy efficient and the CO<sub>2</sub> footprint is low. No additional or tailor-made equipment is necessary for the proposed process, and it can be done using simple processing techniques used in the polymer industry, with a high percentage economy.

### 2. RESULTS AND DISCUSSION

2.1. Morphological Studies. The obtained attenuated total reflection-Fourier transform infrared spectroscopy (ATR-FTIR) spectra and the carbon backbone structure of the inner-filtration layer taken out from medical face masks is given in Figures S1 and S2 and Table S1. The spectra obtained are in good correlation with the ATR-FTIR spectra reported for PP. 29,30 The characteristic peaks obtained near 2900 cm<sup>-1</sup> corresponds to the asymmetric and symmetric stretching vibrations of CH<sub>3</sub> and CH<sub>2</sub> in PP. The other predominant peaks near 1400 cm<sup>-1</sup> correspond to the other asymmetric and symmetric deformation vibrations of CH<sub>3</sub> or/and scissor vibrations of CH<sub>2</sub>. There are various small peaks around 1200 to 700 cm<sup>-1</sup> in the ATR spectra of PP, which correspond to other C-C and C-H stretching vibrations. There are no other peaks corresponding to functional groups with heteroatoms, which confirms that the filter layer is purely made of PP.

The field emission scanning electron microscopy (FE-SEM) images show the morphological structure of the PP filter membrane of the N95 mask and the fracture surface of the PP-NBR blend, shown in Figures 3 and 4, respectively, which

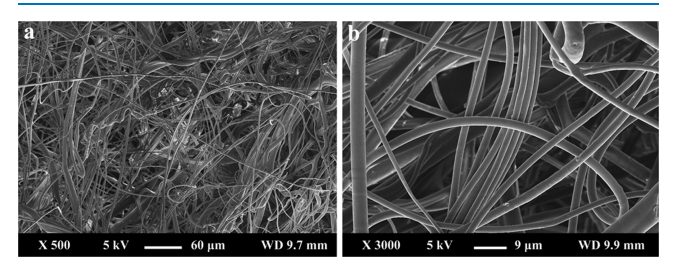
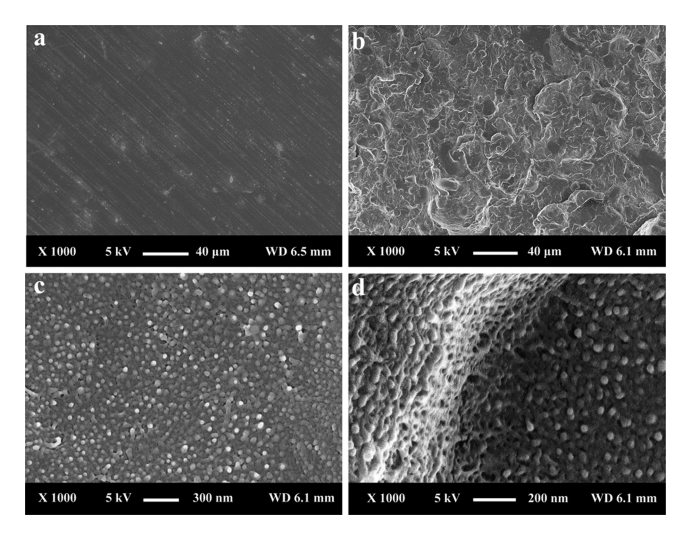


Figure 3. FE-SEM image of the PP filter membrane of the N95 face mask: (a) low resolution and (b) high resolution.

give a vivid information about the presence of wellinterconnected multi-fibrous layers and interstices with ultrafine and fully interconnected pore structures between the fibers. The FE-SEM image of the PP filter membrane (Figure 3) reveals a typical fibrous morphology of the nonwoven PP fiber material with a diameter in the micrometer range, and it can be seen that the interlaying of the fibers generates a highly porous fibrous structure for the melt blown membrane. The filter membrane consists of multi-layered, three-dimensional network structures of ultrafine fibers with a bead-free morphology. The high-resolution FE-SEM images clearly show that the fibers are very smooth and have a very uniform morphology. The histogram and fiber diameter distribution table of PP filter membrane is given in Figure S3 and Table S2, respectively. The fiber diameter of the PP filter membrane is significantly varied from 0.5 to 20  $\mu$ m. All the fibers in the filter membrane exhibit a long and straight fibrous morphology, with an average fiber diameter (AFD) of 3.8  $\mu$ m. Homogenous



**Figure 4.** FE-SEM image of the 70:30 PP-NBR blend: (a) surface topography and the fracture surface at (b) low resolution and (c,d) high resolutions.

mixing and uniform distribution of PP in the blend with no microphase separation is observed in the fracture morphology of the blend (Figure 4), which reveals the enhanced compatibility and better interaction of the PP with NBR, made possible by the interfacial adhesion efficiency of MA.

2.2. Mechanical and Dynamic Mechanical Studies. The variation in the tensile strength and elongation at break of the PP-NBR blend is given in Figure 5. Both ultimate tensile strengths show an increasing trend with the PP content in the blend. From the graph, it is obvious that as the PP content in the blend increases, the tensile strength increases and there is a gradual decrease in the elongation at break. The carbonyl groups in MA give polarity to the surface of the non-polar PP, and the three-dimensional elastomeric network is formed within the blend due to better interfacial interaction of the surface-modified PP with NBR. Additionally, there is sulfur cross-linking within the NBR matrix, which results from the vulcanization process, that again increases the strength of the blend, makes islands of PP within the network structures, and blocks the phase separation, as shown in Figure 6. The tensile strength and elongation at break of the neat NBR is found to be 2.4 MPa and 342.7%, respectively, whereas that for the neat PP is found to be 26.0 MPa and 2.1%, respectively. The reported tensile strength of virgin PP is found to be 35 MPa. 26 Compared to NBR, PP has a higher tensile strength, which also contributes to the trend in the tensile strength of the blends.

The variations in the hardness of the blends are shown in Figure 7. From the plot, it is evident that as the PP content increases, the hardness of the blend increases due to the higher hardness of PP compared to NBR. PP, which is a linear polymer, softens with heat and then gets harder on cooling, which is a typical characteristic property of thermoplastic polymers. The intermolecular forces between the polymer chains are comparatively weaker, or in another words, the polymer chains are held together by weak van der Waals forces in the case of both PP and NBR. The hardness of PP also depends on the tacticity of the polymer because isotactic PP has a much enhanced crystallinity and thus stiffness, compared to syndiotactic and atactic PP, due to the ordered arrangement of polymer chains. Thus, a surge in the PP content increases the hardness of the blend.

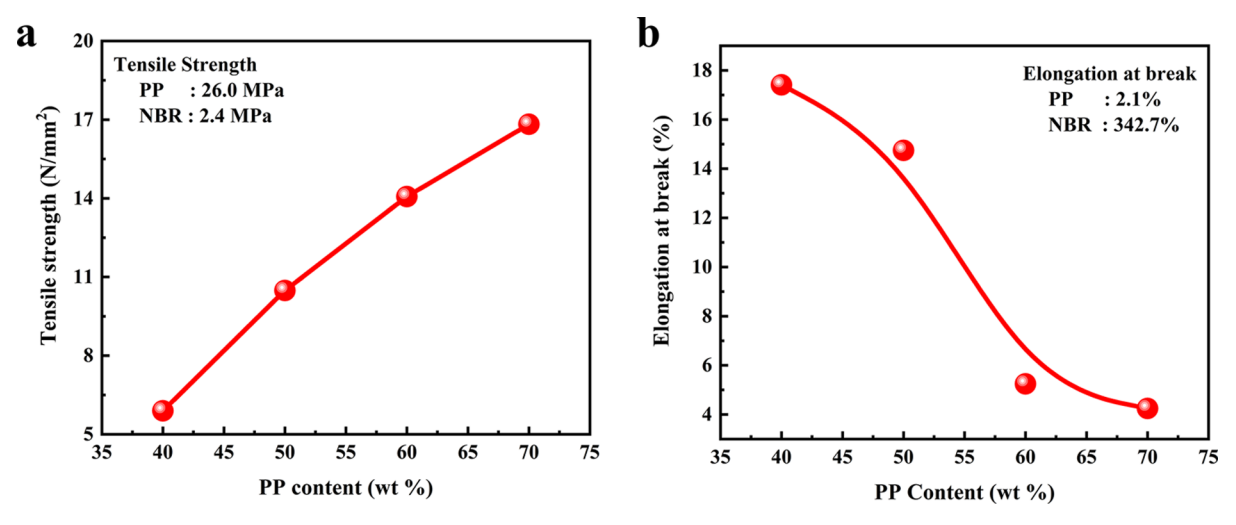


Figure 5. Mechanical properties of the PP-NBR blend with a varying PP content (wt %): (a) tensile strength and (b) elongation at break.

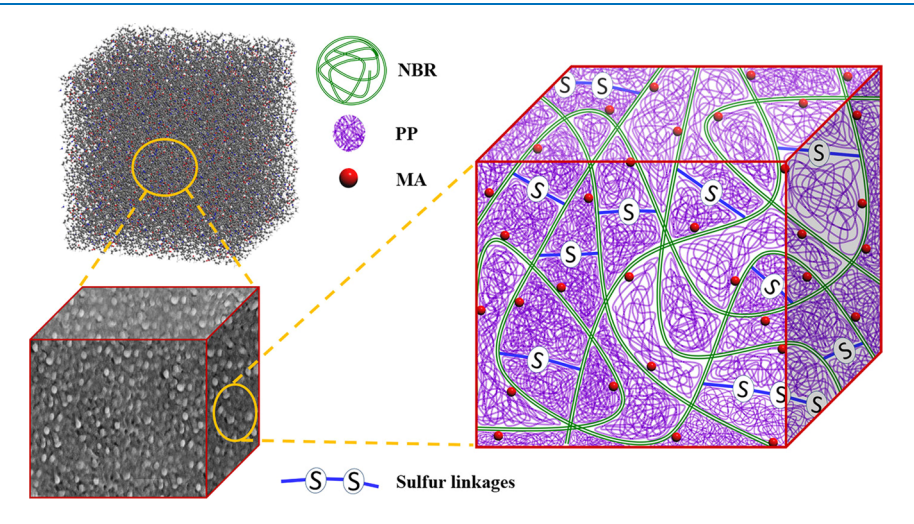


Figure 6. Schematic representation of the formation of the PP-NBR blend with MA.

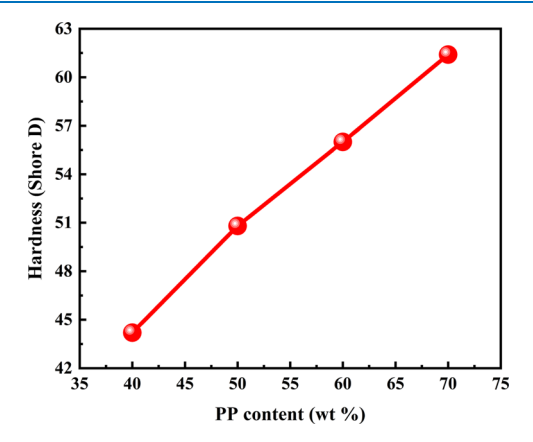


Figure 7. Effect of PP content (wt %) on the hardness (Shore D hardness) of the PP-NBR blend.

The variation in storage modulus and loss modulus as well as the tan  $\delta$  curve obtained from the dynamic mechanical analysis (DMA) is given in Figure 8. The storage modulus is found to decrease as the NBR content is increased because the surged elastic nature is of the NBR counterpart. The opposite can be expected in the case of loss modulus. The blends that are not compatible will give more than one peak in the tan  $\delta$  versus

temperature plot corresponding to the glass transition temperature  $(T_{\rm g})$  of component polymers. If the blend is compatible enough, the resultant peak obtained would be intermediate to the  $T_{\rm g}$  of both monomers. Here, in the tan  $\delta$  versus temperature plot, two peaks are obtained corresponding to the  $T_{\rm g}$  of the PP and NBR, which indicates that the nonpolar PP and polar NBR are immiscible polymers. The broad and intense peak observed at a temperature above 90 °C corresponds to the alpha relaxation of PP. The cross-linking between PP and NBR was made possible by the addition of MA, which acts as an interfacial agent that can anchor the PP and NBR together through chemical bonding, and thus, we obtained increased properties. Therefore, MA acts as an adhesive force between the PP and NBR in the blend.

**2.3. Simulation Studies.** As it was stated above, the allatomistic molecular dynamics simulations were performed to understand the disparity in the interfacial adhesion and compatibility between the PP and NBR phases in the blend. In this regard, a series of MD simulations were carried out, where PP–NBR<sub>(00)</sub> and PP–NBR<sub>(MA)</sub> atomistic models were subjected to geometrical optimization and annealing processes to equilibrate and condition the polymeric system. The equilibrated polymeric systems are virtually tested for mechanical and barrier properties. As the first step, a

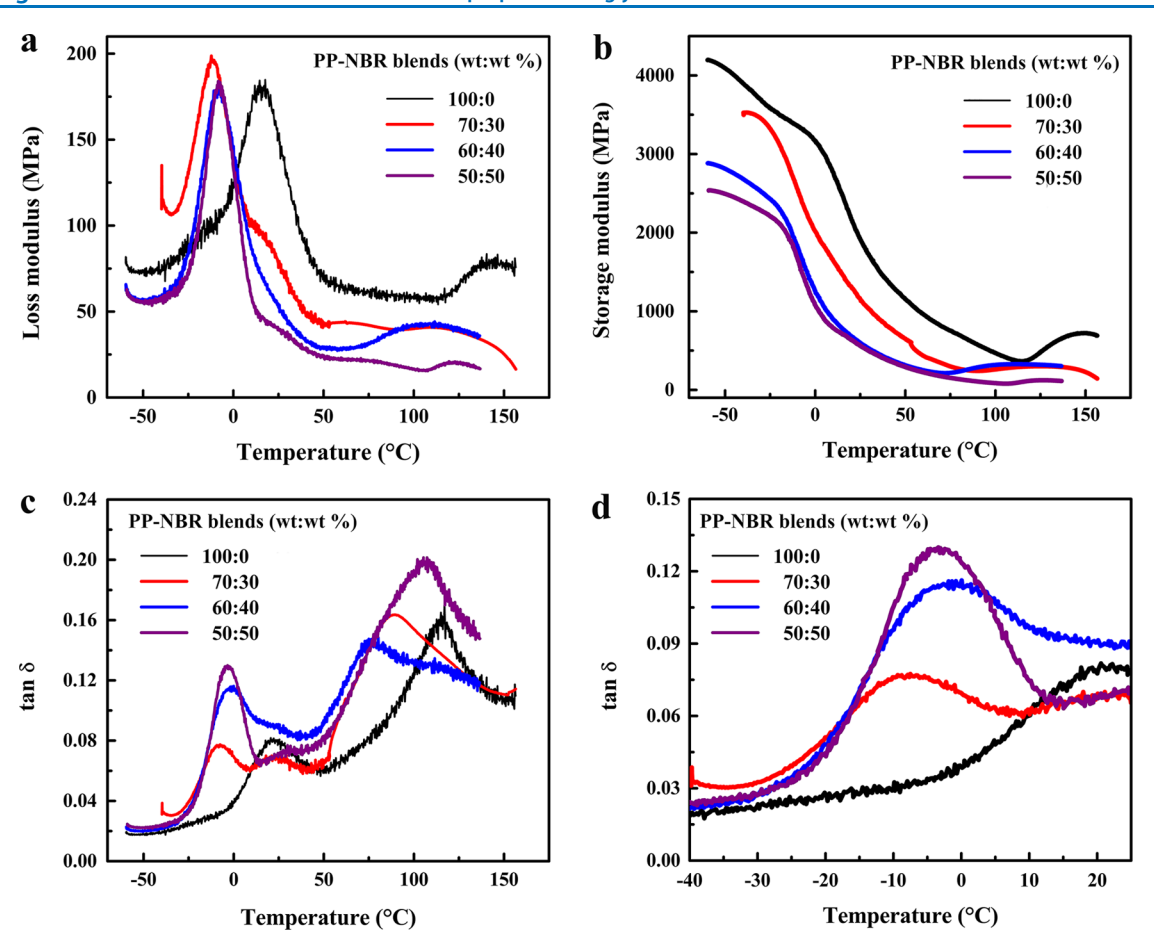


Figure 8. Dynamic mechanical analysis of the PP–NBR blend with a varying PP content (wt %): (a) variation in storage modulus, (b) loss modulus, (c) tan  $\delta$  plot, and (d) highlighted peaks of the tan  $\delta$  curve.

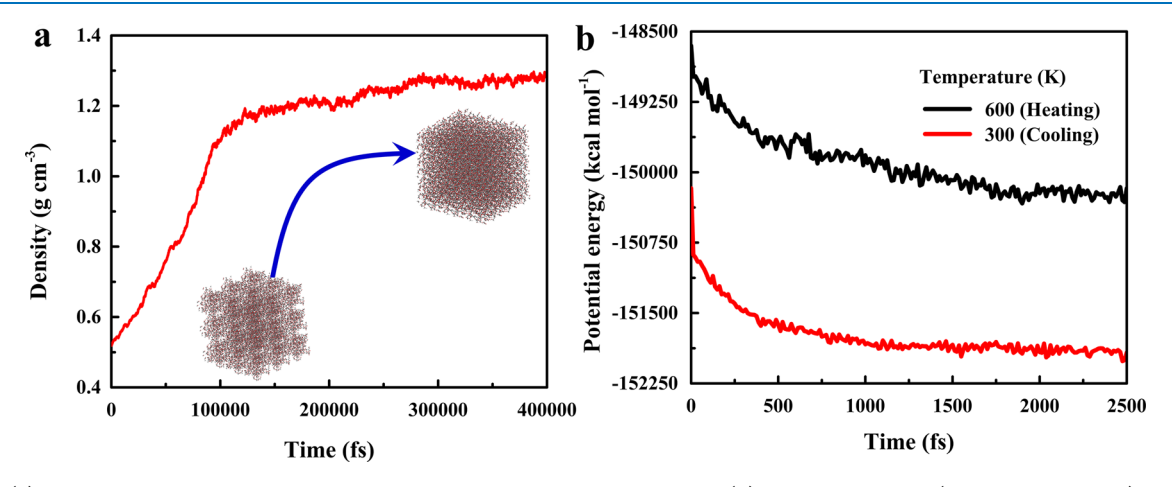


Figure 9. (a) Density vs time plot for density convergence of the PP-NBR blend and (b) annealing process (heating and cooling) for the PP-NBR blend for eliminating heterogeneity in local density.

simulation box with an initial density of 0.5 g cm<sup>-3</sup> was subjected to *NPT* Bredesen dynamics for achieving the realistic density of polymeric materials, as shown in Figure 9a. At each time step, 0.101 MPa pressure was applied to the cuboidal box until the density converges to  $1.22 \pm 0.05$  g cm<sup>-3</sup>. The structural change during density convergence has been depicted in Figure 10, representing the 2D view of the composites, and the corresponding 3D view is given in Figure S4. The final structure after *NPT* dynamics still contains heterogeneity in the local density. The annealing process is

carried out to alleviate the heterogeneity in the local density of the final structure; it involves increasing the temperature of the structure from 300 to 600 K and cooling it down to 300 K. This process is illustrated in Figure 9b.

The obtained annealed structures were then subjected to virtual mechanical testing by unilaterally deforming one axis of the cuboidal simulation box, whereas the other two axes were free to approach each other due to Poisson's effect. The stress–strain behavior of PP–NBR<sub>(MA)</sub> and PP–NBR<sub>(00)</sub> is illustrated in Figure 11; PP–NBR<sub>(MA)</sub> shows a higher tensile

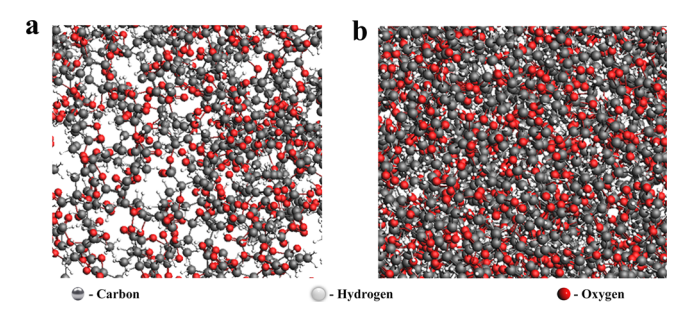


Figure 10. Structural change during the density convergence of the PP-NBR blend; snapshot of molecular packing: (a) before and (b) after density convergence.

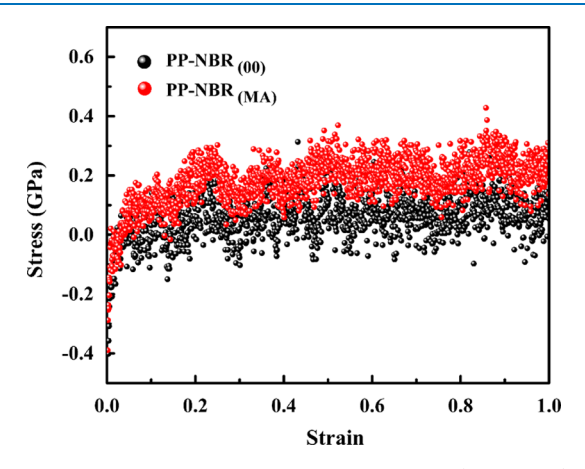


Figure 11. Stress-strain behavior of PP-NBR<sub>(00)</sub> (black dots) and PP-NBR<sub>(MA)</sub> (red dots).

modulus than PP-NBR<sub>(00)</sub>. This manifests that MA grafting improves the interfacial interaction between non-polar PP and polar NBR phases in the blend. The larger fluctuations in the stress-strain graph are due to considerable vibrations that atoms experience at the atomistic level. It can be observed that the MA grafting not only improves the interfacial adhesion between polar and non-polar domains of the blend but also imparts strength and impedes the phase separation.

The diffusibility of the water molecules in PP-NBR(MA) and PP-NBR<sub>(00)</sub> is investigated to analyze the influence of interfacial adhesion on the barrier properties of PP-NBR

blends. The dynamics of the water molecules in PP-NBR blends can be quantified by calculating the mean square displacement (MSD) of the water molecules in the simulated polymer. It is a two-dimensional function and defined as the square of the average distance that the water molecule has moved away from its starting point within the time interval  $\tau$  as given by eq 1. This function contains the diffusivity of observed molecules; the steeper they raise to higher values, the faster the observed particle diffuses in the system. The slope of the MSD will yield the diffusion coefficient of the observed particles, as given in eq 2.

$$MSD(\tau) = \langle |\overrightarrow{r_i}(t+\tau) - \overrightarrow{r_i}(t)|^2 \rangle t, i$$
 (1)

$$D(\tau) = \lim_{\tau \to \infty} \frac{1}{6\tau} \langle |\overrightarrow{r_i}(t+\tau) - \overrightarrow{r_i}(t)|^2 \rangle t, i$$
(2)

where,  $\overrightarrow{r_i}(t+\tau)$  and  $\overrightarrow{r_i}(t)$  are the atomistic positions of the center of mass at initial time t and later time  $t + \tau$ , respectively. From Figure 12a, it can be observed the MSD of water in PP- $NBR_{(00)}$  is higher than in  $PP-NBR_{(MA)}$ .

The MA molecule has oxygen atoms, which can form hydrogen bonding with water molecules and impede its movements through the interstices of the polymer. Figure 12b shows the formation of a higher number of hydrogen bonding in PP-NBR(MA) than in PP-NBR(00). In addition to the propensity of water molecules to form hydrogen bonding with oxygen atom rich MA, the slow diffusion of the water molecules in PP-NBR(MA) can be explained using free volume theory.<sup>32</sup> In PP-NBR<sub>(MA)</sub>, there is a higher interfacial adhesion between PP and NBR phases, and it resists phase separation. This results in a lower free volume for water penetration in PP-NBR(MA). However, at the same time, PP-NBR(00) is susceptible to phase separation, and the presence of a higher free volume facilitates the higher MSD. This elucidates that the compatibilizer of non-polar PP and polar NBR phases in the blend with MA improves the stability and integrity of blends. In consensus with experimental studies, the computational assessment of the PP-NBR blend using atomistic molecular dynamics reveals that the use of the compatibilizer improves the mechanical and barrier properties of the blend.

**2.4. Thermal Studies.** The thermal properties of the PP-NBR blend are studied, and the thermogravimetric analysis (TGA) plot for the neat PP and NBR along with the 70:30 and

150

PP-NBR (00)

200

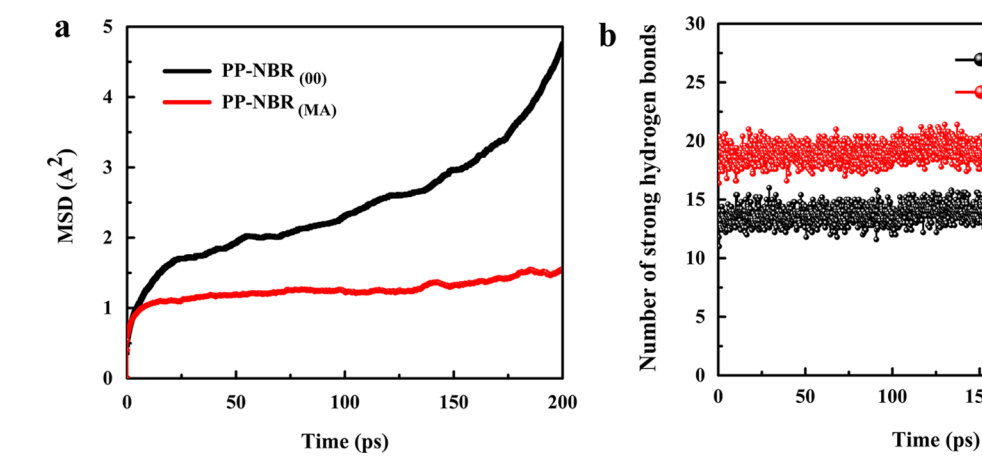


Figure 12. (a) MSD curve behavior of PP-NBR(00) (black dots) and PP-NBR(MA) (red dots); (b) number of strong hydrogen bonds in PP-NBR<sub>(00)</sub> (black dots) and PP-NBR<sub>(MA)</sub> (red dots).

250

60:40 PP-NBR blends are given in Figure 13. It is found that the thermal stability of the blend increases with the increasing

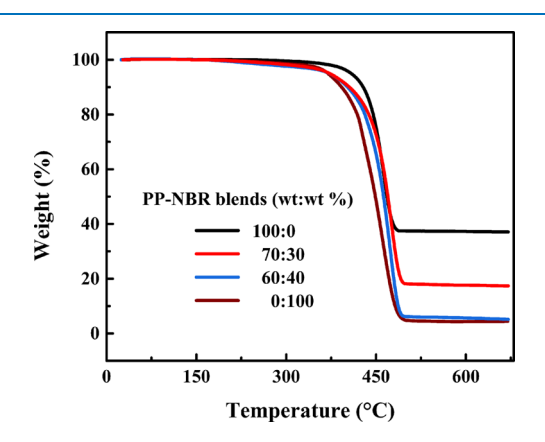


Figure 13. TGA of PP-NBR blends with a varying PP content (wt %).

PP content in the blend. Only one decomposition temperature is observed for all the samples, which indicates the uniformity or compatibility of the blend. The PP—NBR blends have an intermediate thermal stability compared to the component polymers, which corresponds to the cross-linking between PP and NBR polymers that was made possible with the help of MA. This better interfacial adhesion helps in enhancing the thermal stability of the blends.

It can be seen from Figure 13 that the polymer blend is stable up to 400 °C. The TGA curve of PP–NBR does not show any characteristic two-step weight loss corresponding to the decomposition temperature of NBR and PP, which indicates a uniformity in the blending and improved compatibility of PP and NBR. The decomposition peak of the PP–NBR blend is shifted to a higher temperature (415 °C) from that of pristine NBR (390 °C), which indicates the presence of a highly thermally stable PP in the blend. Moreover, this can also be attributed to the better interaction between PP and NBR in the polymer blend, which leads to good mechanical and thermal stability. At a temperature of 488 °C, pristine NBR is completely decomposed.

The decomposition temperature of the blends is in the following order: PP (415 °C) > 70:30 PP–NBR (406 °C) > 60:40 PP–NBR (400 °C) > NBR (390 °C). At 450 °C, the polymer blend shows a weight loss of 34.5 and 28% for the PP–NBR blend having 60 and 70 wt % PP, respectively. From

450 to 480 °C, a weight loss of 51 and 57.2% was observed for the 60:40 and 70:30 PP-NBR blend, respectively, while NBR and PP showed 61 and 62% weight loss, respectively. The decomposition is completed at temperatures of 480, 491, and 494 °C for PP, PP-NBR blend, and NBR, respectively. The char yield at 600 °C is 37.4, 3.9, 6.2, and 17.6%, respectively, for PP, NBR, and 60:40 and 70:30 PP-NBR blends. Compared to the 60:40 PP-NBR blend, the high char yield of the 70:30 PP-NBR blend is attributed to a higher PP content (70 wt %) in the blend. At 600 °C, a char yield of 17.6% is observed for 70:30 PP-NBR blend, which is about 47.6% char yield of pristine PP, proving that the prepared PP-NBR blend has good thermal stability.

2.5. Reaction Mechanism for the PP-NBR Blend Formation. The formation of the PP-NBR blend results from a radical mechanism. DCP acts as an initiator in the overall reaction. Thermal homolytic fission of the unstable oxygen-oxygen single bond (peroxide bond), which is comparatively weaker, as well as the high energy bond occurs mainly due to the repulsion between two electron-rich clouds of electronegative oxygen atoms, as shown in Scheme 1. As a result, cumyloxy radicals are formed as the primary intermediate radical, which are extremely unstable. Further, the primary intermediate radical undergoes  $\beta$ -scission, which is the cumulative effect of the breaking of the weakest carboncarbon bond and the scission of the bulkier fragment due to steric effect. The bond toward tertiary carbon will be cleaved rather than the bonds toward the primary and secondary carbons because the tertiary free radicals formed are stable intermediates. Here, the cumyloxy radicals undergo  $\beta$ -scission, which results in secondary fragmentation into methyl radical and acetophenone. The methyl radical of the primary radical will be the trigger for the further cross-linking mechanism of the PP-NBR blend. The decomposition of peroxide follows first-order kinetics and is also the rate-determining step of the overall process.33

In the next step, the methyl intermediate radical, which is highly reactive and a good hydrogen abstractor based on its parent hydrogen bond dissociation energy as well as less steric hindrance, will abstract the  $\alpha$ -hydrogen from the PP, as shown in Scheme 2. The resultant would be the PP intermediate radical along with methane as the byproduct. The formation of methane, which is a marsh gas, is evident from the irritating sensation and white fumes produced during the reaction process, which can be the result of the reduction in the oxygen

Scheme 1. Thermal Decomposition of DCP

$$H_{3}C$$
 $CH_{3}$ 
 $CH_{3}$ 
 $CH_{3}$ 
 $CH_{3}$ 
 $CH_{3}$ 
 $CH_{3}$ 
 $CH_{3}$ 

Scheme 2. Reaction Mechanism for the Formation of PP Intermediate Radical

Scheme 3. Reaction Mechanism for the Formation of the MA-Modified PP

content in air<sup>34</sup> and the increase in the concentration of carbon dioxide and water.

The formed PP intermediate radical will abstract hydrogen from the carbon–carbon  $\pi$ -bond of MA, forming a MA-grafted PP intermediate radical, and may further undergo a disproportionation reaction forming two different molecules, which in general is called MA-modified PP, as shown in Scheme 3. Due to the strong electron-accepting capability of the MA-grafted PP intermediate radical, it prefers to undergo disproportion rather than coupling between two MA-grafted PP intermediate radicals.<sup>35</sup> Further, the MA-grafted PP intermediate radicals are unstable, and due to the steric hindrance, the possibility for the disproportionation sounds higher rather than making another molecule to get attached to them. Proceeding the reaction mechanism using the two obtained MA-modified PP molecules is equally possible. The reaction mechanism using the first product is discussed further. Likewise, the second one.

In the final step, the MA-modified PP will react with NBR. There are two possibilities for the MA-modified PP to abstract hydrogen from the two lethal allylic hydrogens of the NBR polymer chain. The carbanion formed from the allylic carbon is more stable than the carbanion formed from the  $\alpha$ -carbon, which supports the statement of attacking the MA-modified PP on lethal allylic hydrogens of NBR. The reaction mechanism toward the PP–NBR blend through the two expected possibilities are explained (method I and method II) in Scheme 4. Both the mechanism proceeds through the formation of secondary carbanion as the intermediate. The MA-modified PP will not attack the carbon in the –CN group

of NBR because the molecules are bulky polymer chains; there will be extreme steric hindrance as well as the electron-rich cloud of -CN group will repel the lone pair of electrons in the oxygen atom of the MA-modified PP, which reduces the chances for the MA-modified PP to attack the carbon in the -CN group of NBR. Further, it is expected that the MAmodified PP will not attack the  $\alpha$ -carbon, so that the intermediate formed is tertiary carbanion. Because the tertiary carbanion is less stable than secondary carbanion (in the case of allylic carbon), the lone pairs of electrons on the oxygen atom of the MA-modified PP will prefer to abstract hydrogen from the allylic carbon rather than the hydrogen from the  $\alpha$ carbon. Moreover, the carbanion formed will attack the carbonyl carbon of the MA-modified PP, which results in ring opening of the MA-modified PP moiety, causing the -OH group to get stabilized, thus resulting in PP-NBR blends.<sup>36</sup>

The vulcanization of NBR is separately done in which sulfur curing will result in sulfur cross-linking within the NBR matrix, forming a three-dimensional elastomeric network, which will strengthen the NBR counterpart and thus add on to the enhanced mechanical properties of PP–NBR blends. ZnO and stearic acid undergo in situ reaction and form zinc stearate, which helps in activating the accelerator system to provide an increased cross-linking density. Stearic acid also acts as a softener for the rubber chains and enhances the mixing. The accelerator system used is a combination of primary and secondary accelerators, N-cyclohexyl-2-benzothiazolesulfenamide (CBS)—tetramethylthiuramdisulphide (TMTD), which fastens the accelerator action through its synergistic effect. For

Scheme 4. Reaction Mechanism for the Formation of the PP-NBR Blend

comparison and as evidence, the ATR-FTIR spectra of PP, NBR, MA, and 70:30 PP-NBR blend are given in Figure S1.

### 3. CONCLUSIONS

The presented work demonstrates a novel and potential scientific method for the recycling of medical face masks by blending non-polar PP taken from the N95 mask with polar NBR using MA as the compatibilizer. The ATR spectra obtained for PP are in good correlation with the reported spectra. The fibrous morphology of nonwoven PP is also in good agreement with the FE-SEM results. The mechanical properties like tensile strength and elongation at break of the blends increase as the PP content is increased, and likewise the hardness, and this can be due to the network formation within the blend. From the DMA results, the tan  $\delta$  versus temperature plot gives two peaks corresponding to the  $T_{\rm g}$  of each monomer, and this indicates that MA will act as an interfacial agent and anchor for the PP and NBR together rather than

making PP and NBR miscible. The PP-NBR blends have an intermediate thermal stability compared to neat PP and NBR due to better interfacial adhesion between PP and NBR. In addition, all-atomistic molecular dynamics simulations were performed to understand the disparity in the interfacial adhesion and compatibility between the PP and NBR phases in the blend. The simulations were in good agreement with experimental characterization data, where MD simulations of PP-NBR blends showed that the MA compatibilizer improves the mechanical and barrier properties of PP-NBR blends. This can be accounted for by the improved interfacial adhesion and stability of the PP-NBR blend. The compatibilization between non-polar PP and polar NBR phases is vitally important for increasing the interfacial adhesion and impeding the phase separation. Thus, the PP-NBR blend, which envisaged a method for the recycling of the medical waste to a value-added product, would be a boon for the environment as well as for the general population and will lead to the development of an

engineering product from the trash for remarkable applications.

#### 4. EXPERIMENTAL SECTION

**4.1. Materials.** Nonwoven PP filter layers were taken from disinfected N95 masks. NBR with an ACN content of 32–36% (KNB 35L) was purchased from Kumho Petrochemicals Co. Ltd, Korea. MA as the interfacial agent (compatibilizer), TMTD as the accelerator, zinc oxide (ZnO) and stearic acid as activators, and DCP and sulfur as rubber-grade chemicals were purchased from Sigma-Aldrich Chemicals. CBS, which acts as the primary accelerator, was purchased from NOCIL Ltd.

**4.2. Preparation of the PP-NBR Blend.** Foremost, the infected mask was kept in a hanging position under extreme sunlight for 72 h with full surface area exposure followed by thorough washing for 1.5 h using detergent in a laundry machine (IFB front loaded) and then treated by soaking in alcohol (isopropyl alcohol) for 1 h prior to oven drying at 60 °C for 24 h for ensuring that the mask was disinfected properly. The mask was then cut open and PP filter layers were separated and shredded, followed by the modification of PP with MA and DCP at 180 °C using a Brabender internal mixer. An NBR master batch was prepared separately using an open two-roll mill. A series of blends with MA-modified PP and NBR master batch were then prepared with a varying PP content of 40–70 wt %, as given in Table 1. The test samples

Table 1. Formulation of the PP-NBR Blend

	Composition for PP <sup>a</sup> -NBR blend (php <sup>b</sup> )			
Ingredients	70/30	60/40	50/50	40/30
PP	70	60	50	40
NBR	30	40	50	30
ZnO	5	5	5	5
Stearic acid	2	2	2	2
CBS	1	1	1	1
TMTD	0.3	0.3	0.3	0.3
Sulfur	1.5	1.5	1.5	1.5

<sup>a</sup>PP: MA-modified PP. <sup>b</sup>php: parts per hundred polymers.

were compression molded at  $180\,^{\circ}$ C. Neat NBR and PP test samples (controlled samples) were also prepared under the same conditions. PP was modified with 4 wt % MA and 0.8 wt % DCP.

4.3. Simulation of the PP-NBR Blend with and without MA. The all-atomistic molecular dynamics simulations were performed to understand the disparity in the interfacial adhesion and compatibility between the PP and NBR phases in the blend. Two molecular models of PP-NBR blends with and without compatibilizer were created using the Amsterdam density functional (ADF 2019.305) program.<sup>38</sup> The integrated graphical user interface allows the atomistic model building of PP-NBR systems. The polymer builder tool in the ADF was utilized to create 10 repeating units of both PP and NBR chains separately. The PP-NBR blend without the compatibilizer (PP-NBR<sub>00</sub>) was created by packing 50 PP chains and 50 NBR chains in the simulation box. The PP-NBR blend with the compatibilizer (PP-NBR<sub>MA</sub>) was created by grafting one PP chain with one NBR chain using MA. Fifty chains of grafted PP-NBR chains were packed in the simulation box. In both instances, the polymeric chains were packed using the builder tool in the ADF program at an initial

packing density of 0.5 g cm<sup>-3</sup>. A long geometrical optimization of 10,000 steps and initial relaxation of the system were carried out using the force field based on the functionalized hydrocarbons/water weak interactions in a condensed phase (CHNO2017\_weak) present in the ReaxFF module in the ADF program.<sup>39</sup> To reduce the local heterogeneity of the simulated polymeric system, the annealing was carried out by heating the polymer from 26.9 °C (300 K) to 326.9 °C (600 K) and then cooling it back to 26.9 °C (300 K). After the annealing process, the *NPT* simulations were carried out for 400 ps with 0.25 fs time step for converging the density to a realistic density of polymeric materials of 1.22  $\pm$  0.05 g cm<sup>-3</sup>. The polymer that formed at the end of the *NPT* simulation is shown in Figure 14a,b.

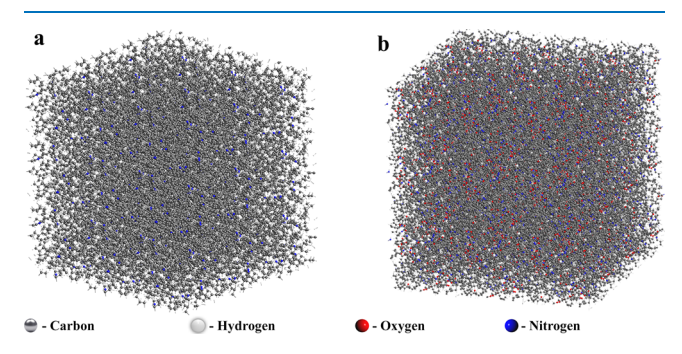


Figure 14. Snapshot of the bulk simulation box consisting of (a) PP–NBR $_{(00)}$  and (b) PP–NBR $_{(MA)}$ .

Different simulation strategies were used to measure the stress-strain properties and water diffusion properties of PP-NBR<sub>(MA)</sub> and PP-NBR<sub>(00)</sub>. Higher strain rates were used to calculate the stress-strain properties in MD simulation. 40 The strain rate of  $2 \times 10^8 \text{ s}^{-1}$  was used to deform the cuboidal simulation box unilaterally with the constraint that the box shape remains cuboidal. The NPT Bredesen dynamics were carried out for 4 ns with a 0.25 ps time step at 300 K temperature and 0.1 MPa. Once the calculation was finished, the stress-strain curves could be extracted from the binary results file with the help of a Python script using the PLAMS library in the ADF program.<sup>32</sup> For measuring the diffusion of a water molecule in PP-NBR(MA) and PP-NBR(00), 10 molecules of water were inserted by adding a solvent molecule tool in the ADF program. The radius of the solvent sphere and solute factor was adjusted to fill the interstice of PP-NBR models with 10 molecules of water. The NPT dynamics simulation was carried out at 600 K and 0.1 MPa for 500 ps with 0.25 fs time step to equilibrate the system. The density started to fluctuate and attained an equilibrium density for a given temperature and pressure. A configuration with the density closest to the equilibrium value was then used to initiate NVT ensemble dynamics for a period of 2 ns with 0.25 fs time step at 600 K and 0.1 MPa. The binary rxkf file from the NVT dynamics simulation was converted into a non-back translated xyz trajectory for use with TRAVIS for trajectory analysis. 41 The MSD of a water molecule through the interstice of PP-NBR models was evaluated using TRAVIS. 42 A higher temperature was employed to simulate the faster dynamics of water in the PP-NBR models, which corresponds to the virtual glassy nature of simulated models.

**4.4.** Characterization of the PP-NBR Blend. 4.4.1. Fourier Transform Infrared Spectroscopy. The material

identification of PP was done using ATR-FTIR (PerkinElmer Spectrum Two), performed at room temperature, which make use of infrared radiation to examine the sample. The stretching and bending vibrations of various bonds within the molecule give the corresponding peaks in our ATR spectra, and thus, its chemical structure can be confirmed, because the multi-layered medical face mask contains more than one material.

4.4.2. Field Emission Scanning Electron Microscopy. The fiber morphology of the PP filter membrane and the fracture surface of the PP—NBR blend were recorded with high-resolution FE-SEM (Carl Zeiss Supra 40 VP) at an accelerating voltage of 5 kV, which envisages the topographic details on the surface. The samples for FE-SEM imaging were mounted on metal stubs using a conductive double-sided carbon tape, and a thin layer of gold was sputtered on the sample using a sputter-coating machine (JEOL JFC-1200) prior to scanning at a current of 10 mA for 100 s, which enhances the conductivity over the surface of the sample and thus increases the signal-tonoise ratio.

4.4.3. Average Fiber Diameter. The AFD of the sample was estimated over about 300 fibers from the micrograph taken at a high magnification.

4.4.4. Mechanical Characterization. The slabs for tensile samples were carefully compression molded on an electrically heated hydraulic press having 45 × 45 cm² platen at a pressure of 200 kg cm² at 180 °C. Samples were conditioned at room temperature for 24 h before tensile testing. Tensile tests were carried out on a Shimadzu Model AGI universal testing machine (UTM; UTB-T-72052-HiTech) using test specimens punched out from the molded slab using a dumbbell-shaped mold. The measurements were taken at a cross-head speed of 500 mm min¹. The hardness was studied using the Shore D durometer (MODEX 3061) with a sample thickness of nearly 10 mm at room temperature.

4.4.5. Dynamic Mechanical Analysis. The viscoelastic properties were studied using DMA Q800 with a sample dimension of 60 mm in the temperature range of -60 to 150 °C with a ramp of 5 °C min<sup>-1</sup>, working at a frequency of 1 Hz and an amplitude of 15  $\mu$ m in a dual cantilever.

4.4.6. Thermogravimetric Analyzer. The thermal properties of the PP fiber, NBR, and PP–NBR blends were recorded using TGA Q-50 under  $N_2$  atmosphere within the temperature range from room temperature to 800 °C with a ramp of 20 °C min<sup>-1</sup> that measures the weight changes as a function of temperature.

## ASSOCIATED CONTENT

## Supporting Information

The Supporting Information is available free of charge at https://pubs.acs.org/doi/10.1021/acsomega.1c04913.

Detailed explanation of the ATR-FTIR spectra; PP, MA, NBR, and PP-NBR blends; the AFD along with the fiber diameter distribution table and histogram of the PP filtration layer of the N95 mask; and snapshots of molecular packing (3D view of the sample before and after density convergence) (PDF)

#### AUTHOR INFORMATION

#### **Corresponding Authors**

Bakhtiyor Rasulev — Department of Coatings and Polymeric Materials, North Dakota State University, Fargo, North Dakota 58105, United States; o orcid.org/0000-0002-7845-4884; Email: bakhtiyor.rasulev@ndsu.edu

Prasanth Raghavan — Materials Science and NanoEngineering Lab, Department of Polymer Science and Rubber Technology, Cochin University of Science and Technology (CUSAT), Kochi 682022 Kerala, India; Department of Materials Engineering and Convergence Technology, Gyeongsang National University, Jinju 52828, Republic of Korea; orcid.org/0000-0002-9888-665X; Email: prasanth@cusat.ac.in

#### **Authors**

George Varghese P. J – Department of Metallurgical and Materials Engineering, Indian Institute of Technology Patna (IIT P), Patna 801106 Bihar, India; Materials Science and NanoEngineering Lab, Department of Polymer Science and Rubber Technology, Cochin University of Science and Technology (CUSAT), Kochi 682022 Kerala, India; orcid.org/0000-0001-6481-1548

Deepthi Anna David – Materials Science and NanoEngineering Lab, Department of Polymer Science and Rubber Technology, Cochin University of Science and Technology (CUSAT), Kochi 682022 Kerala, India; Department of Applied Chemistry, Cochin University of Science and Technology (CUSAT), Kochi 682022 Kerala, India; orcid.org/0000-0003-2178-285X

Anas Karuth – Department of Coatings and Polymeric Materials, North Dakota State University, Fargo, North Dakota 58105, United States

Jabeen Fatima Manamkeri Jafferali — Materials Science and NanoEngineering Lab, Department of Polymer Science and Rubber Technology, Cochin University of Science and Technology (CUSAT), Kochi 682022 Kerala, India; orcid.org/0000-0002-9537-9388

Sabura Begum P. M – Department of Applied Chemistry, Cochin University of Science and Technology (CUSAT), Kochi 682022 Kerala, India; ⊚ orcid.org/0000-0002-1915-2325

Jinu Jacob George — Materials Science and NanoEngineering Lab, Department of Polymer Science and Rubber Technology, Cochin University of Science and Technology (CUSAT), Kochi 682022 Kerala, India

Complete contact information is available at: https://pubs.acs.org/10.1021/acsomega.1c04913

#### **Author Contributions**

The manuscript was written through contributions of all authors. All authors have given approval to the final version of the manuscript.

#### Notes

The authors declare no competing financial interest.

#### ACKNOWLEDGMENTS

The authors Dr. J.F.M.J. and Prof. P.R. greatly acknowledge the government of Kerala for providing financial assistance through the Kerala State Higher Education Council (KSHEC) and the Kerala State Council for Science, Technology and Environment (KSCSTE). This work was supported in part by the National Science Foundation through the ND EPSCoR award #IIA-1355466 and by the State of North Dakota. This work used resources of the Center for Computationally Assisted Science and Technology (CCAST) at North Dakota

State University, which were made possible in part by NSF MRI Award No. 2019077. Authors also thank the Extreme Science and Engineering Discovery Environment (XSEDE) for the award allocation (TGDMR110088).

#### REFERENCES

- (1) Benson, N. U.; Bassey, D. E.; Palanisami, T. COVID Pollution: Impact of COVID-19 Pandemic on Global Plastic Waste Footprint. *Heliyon* **2021**, *7*, No. e06343.
- (2) Tripathi, A.; Tyagi, V. K.; Vivekanand, V.; Bose, P.; Suthar, S. Challenges, Opportunities and Progress in Solid Waste Management during COVID-19 Pandemic. *Case Stud. Chem. Environ. Eng.* **2020**, 2, 100060
- (3) Fadare, O. O.; Okoffo, E. D. Covid-19 Face Masks: A Potential Source of Microplastic Fibers in the Environment. *Sci. Total Environ.* **2020**, 737, 140279.
- (4) Patrício Silva, A. L.; Prata, J. C.; Walker, T. R.; Duarte, A. C.; Ouyang, W.; Barcelò, D.; Rocha-Santos, T. Increased Plastic Pollution Due to COVID-19 Pandemic: Challenges and Recommendations. *Chem. Eng. J.* **2021**, 405, 126683.
- (5) Aragaw, T. A. Surgical Face Masks as a Potential Source for Microplastic Pollution in the COVID-19 Scenario. *Mar. Pollut. Bull.* **2020**, *159*, 111517.
- (6) Ilyas, S.; Srivastava, R. R.; Kim, H. Disinfection Technology and Strategies for COVID-19 Hospital and Bio-Medical Waste Management. *Sci. Total Environ.* **2020**, *749*, 141652.
- (7) Battegazzore, D.; Cravero, F.; Frache, A. Is It Possible to Mechanical Recycle the Materials of the Disposable Filtering Masks? *Polymers* **2020**, *12*, 2726.
- (8) Jain, S.; Yadav Lamba, B.; Kumar, S.; Singh, D. Strategy for Repurposing of Disposed PPE Kits by Production of Biofuel: Pressing Priority amidst COVID-19 Pandemic. *Biofuels* **2020**, 1–5.
- (9) Torres, F. G.; De-la-Torre, G. E. Face Mask Waste Generation and Management during the COVID-19 Pandemic: An Overview and the Peruvian Case. *Sci. Total Environ.* **2021**, *786*, 147628.
- (10) Celina, M. C.; Martinez, E.; Omana, M. A.; Sanchez, A.; Wiemann, D.; Tezak, M.; Dargaville, T. R. Extended Use of Face Masks during the COVID-19 Pandemic Thermal Conditioning and Spray-on Surface Disinfection. *Polym. Degrad. Stab.* **2020**, *179*, 109251.
- (11) Czubryt, M. P.; Stecy, T.; Popke, E.; Aitken, R.; Jabusch, K.; Pound, R.; Lawes, P.; Ramjiawan, B.; Pierce, G. N. N95 Mask Reuse in a Major Urban Hospital: COVID-19 Response Process and Procedure. *J. Hosp. Infect.* **2020**, *106*, 277–282.
- (12) Saini, V.; Sikri, K.; Batra, S. D.; Kalra, P.; Gautam, K. Development of a Highly Effective Low-Cost Vaporized Hydrogen Peroxide-Based Method for Disinfection of Personal Protective Equipment for Their Selective Reuse during Pandemics. *Gut Pathog.* **2020**, *12*, 29.
- (13) Weiss, M. M.; Weiss, P. D.; Weiss, D. E.; Weiss, J. B. Disrupting the Transmission of Influenza A: Face Masks and Ultraviolet Light as Control Measures. *Am. J. Public Health* **2007**, *97*, S32–S37.
- (14) Crespo, C.; Ibarz, G.; Sáenz, C.; Gonzalez, P.; Roche, S. Study of Recycling Potential of FFP2 Face Masks and Characterization of the Plastic Mix-Material Obtained. A Way of Reducing Waste in Times of Covid-19. *Waste Biomass Valorization* **2021**, *12*, 6423.
- (15) Hisham, A. Maddah. Polypropylene as a Promising Plastic: A Review. Am. J. Polym. Sci. 2016, 6, 1–11.
- (16) Dunn, J. R.; Coulthard, D. C.; Pfisterer, H. A. Advances in Nitrile Rubber Technology. *Rubber Chem. Technol.* **1978**, *51*, 389–405.
- (17) Maroufkhani, M.; Katbab, A.; Liu, W.; Zhang, J. Polylactide (PLA) and Acrylonitrile Butadiene Rubber (NBR) Blends: The Effect of ACN Content on Morphology, Compatibility and Mechanical Properties. *Polymer* **2017**, *115*, 37–44.
- (18) Pazur, R. J.; Cormier, J. G.; Korhan-Taymaz, K. The Effect of Acrylonitrile Content on the Thermo-oxidative Aging of Nitrile Rubber. *Rubber Chem. Technol.* **2014**, *87*, 53–69.

- (19) Achary, P. S.; Ramaswamy, R. Reactive Compatibilization of a Nitrile Rubber/Phenolic Resin Blend: Effect on Adhesive and Composite Properties. *J. Appl. Polym. Sci.* **1998**, *69*, 1187–1201.
- (20) Ismail, H.; Galpaya, D.; Ahmad, Z. The Compatibilizing Effect of Epoxy Resin (EP) on Polypropylene (PP)/Recycled Acrylonitrile Butadiene Rubber (NBRr) Blends. *Polym. Test.* **2009**, *28*, 363–370.
- (21) Zhang, X.; Huang, H.; Zhang, Y. Dynamically Vulcanized Nitrile Rubber/Polypropylene Thermoplastic Elastomers. *J. Appl. Polym. Sci.* **2002**, *85*, 2862–2866.
- (22) Karuth, A.; Alesadi, A.; Xia, W.; Rasulev, B. Predicting Glass Transition of Amorphous Polymers by Application of Cheminformatics and Molecular Dynamics Simulations. *Polymer* **2021**, *218*, 123495
- (23) Chen, M.; Jabeen, F.; Rasulev, B.; Ossowski, M.; Boudjouk, P. A computational structure-property relationship study of glass transition temperatures for a diverse set of polymers. *J. Polym. Sci., Part B: Polym. Phys.* **2018**, *56*, 877–885.
- (24) Kucukpinar, E.; Doruker, P. Molecular Simulations of Gas Transport in Nitrile Rubber and Styrene Butadiene Rubber. *Polymer* **2006**, *47*, 7835–7845.
- (25) Sahputra, I. H.; Alexiadis, A.; Adams, M. J. Temperature dependence of the Young's modulus of polymers calculated using a hybrid molecular mechanics-molecular dynamics method. *J. Phys. Condens. Matter* **2018**, *30*, 355901.
- (26) George, S.; Joseph, R.; Thomas, S.; Varughese, K. T. Blends of Isotactic Polypropylene and Nitrile Rubber: Morphology, Mechanical Properties and Compatibilization. *Polymer* **1995**, *36*, 4405–4416.
- (27) George, S.; Ramamurthy, K.; Anand, J. S.; Groeninckx, G.; Varughese, K. T.; Thomas, S. Rheological Behaviour of Thermoplastic Elastomers from Polypropylene/Acrylonitrile-Butadiene Rubber Blends: Effect of Blend Ratio, Reactive Compatibilization and Dynamic Vulcanization. *Polymer* 1999, 40, 4325–4344.
- (28) George, S.; Neelakantan, N. R.; Varughese, K. T.; Thomas, S. Dynamic Mechanical Properties of Isotactic Polypropylene/Nitrile Rubber Blends: Effects of Blend Ratio, Reactive Compatibilization, and Dynamic Vulcanization. *J. Polym. Sci., Part B: Polym. Phys.* **1997**, 35, 2309–2327.
- (29) Akbar, D.; Altan, H. Characterization of Polypropylene Treated under Dual-RF Plasma Using Terahertz Time-Domain Spectroscopy. *J. Mater. Sci.* **2013**, *48*, 8209–8214.
- (30) Fang, S.; Meng, Y.; Shen, J.; Cong, J. Surface Treatment of Polypropylene Powders Using a Plasma Reactor with a Stirrer. *Plasma Sci. Technol.* **2011**, *13*, 217–222.
- (31) Jayanarayanan, K.; Thomas, S.; Joseph, K. Morphology, Static and Dynamic Mechanical Properties of in Situ Microfibrillar Composites Based on Polypropylene/Poly (Ethylene Terephthalate) Blends. *Composites, Part A* **2008**, *39*, 164–175.
- (32) PLAMS, SCM. Theoritical Chemistry; Vrije Universiteit, Amsterdam, The Netherlands, 2019.
- (33) Kruželák, J.; Sýkora, R.; Hudec, I. Vulcanization of Rubber Compounds with Peroxide Curing Systems. *Rubber Chem. Technol.* **2017**, *90*, 60–88.
- (34) Bhasin, N.; Mittal, V.; Sood, R. A Fatal Case of Septic Tank Gas Poisoning: Critical Care Challenges. *J. Anesth. Crit. Care* **2016**, *6*, 00228.
- (35) Gaylord, N. G.; Mehta, R.; Kumar, V.; Tazi, M. High Density Polyethylene-g-Maleic Anhydride Preparation in Presence of Electron Donors. *J. Appl. Polym. Sci.* **1989**, *38*, 359–371.
- (36) Ismail, H.; Supri; Yusof, A. M. M. Blend of Waste Poly(Vinylchloride) (PVCw)/Acrylonitrile Butadiene-Rubber (NBR): The Effect of Maleic Anhydride (MAH). *Polym. Test.* **2004**, 23, 675–683.
- (37) Anas, K.; David, S.; Babu, R. R.; Selvakumar, M.; Chattopadhyay, S. Energy Dissipation Characteristics of Crosslinks in Natural Rubber: An Assessment Using Low and High-Frequency Analyzer. J. Polym. Eng. 2018, 38, 723–729.
- (38) te Velde, G.; Bickelhaupt, F. M.; Baerends, E. J.; Fonseca Guerra, C.; van Gisbergen, S. J. A.; Snijders, J. G.; Ziegler, T. Chemistry with ADF. *J. Comput. Chem.* **2001**, 22, 931–967.

- (39) Zhang, W.; Van Duin, A. C. T. Improvement of the ReaxFF Description for Functionalized Hydrocarbon/Water Weak Interactions in the Condensed Phase. *J. Phys. Chem. B* **2018**, *122*, 4083–4092.
- (40) Vashisth, A.; Ashraf, C.; Bakis, C. E.; van Duin, A. C. T. Effect of Chemical Structure on Thermo-Mechanical Properties of Epoxy Polymers: Comparison of Accelerated ReaxFF Simulations and Experiments. *Polymer* **2018**, *158*, 354–363.
- (41) Islam, M. M.; Ostadhossein, A.; Borodin, O.; Yeates, A. T.; Tipton, W. W.; Hennig, R. G.; Kumar, N.; Van Duin, A. C. T. ReaxFF Molecular Dynamics Simulations on Lithiated Sulfur Cathode Materials. *Phys. Chem. Chem. Phys.* **2015**, *17*, 3383–3393.
- (42) Brehm, M.; Kirchner, B. TRAVIS A Free Analyzer and Visualizer for Monte Carlo and Molecular Dynamics Trajectories. *J. Chem. Inf. Model.* **2011**, *51*, 2007–2023.

## **□** Recommended by ACS

Graphene and Hexagonal Boron Nitride in Molybdenum Disulfide/Epoxy Composites for Significant X-ray Shielding Enhancement

Le Yu, Dusan Losic, et al.

AUGUST 19, 2022

ACS APPLIED NANO MATERIALS

READ **Z** 

Fire Propagation Behavior of Some Biobased Furanic Compounds with a Focus on the Polymer PEF

Anitha Muralidhara, Guy Marlair, et al.

MARCH 14, 2022

ACS OMEGA

READ **Z** 

Development of the Antithrombotic Peptide LEKNSTY Targeting the Collagen Surface: I. Design and Validation

Si Zheng, Lin Zhang, et al.

MAY 27, 2022 LANGMUIR

READ 🗹

Molecular Simulations of Thermomechanical Properties of Epoxy-Amine Resins

Mathilde Orselly, Patrice Malfreyt, et al.

AUGUST 22, 2022

ACS OMEGA

READ 🗹

Get More Suggestions >